Talbot laser for Airy pulse generation

M. Cuenca*, H. Maestre, and C. R. Fernández-Pousa

Engineering Research Institute I3E, Universidad Miguel Hernández, Av. Universidad s/n, E03203 Elche, Spain

E-mail: miguel.cuenca02@goumh.umh.es

Abstract. We report a C-band fiber Talbot laser –an injection-seeded frequency-shifting active ring cavity operated above threshold– emitting trains of far-field Airy pulses characterized by a dominant cubic spectral phase. Pulses are created by the coherent addition of the recirculating seed wavelength under a large roundtrip first-order dispersion. Single-sided Airy pulse trains with sub-ns pulse widths, 80-MHz repetition rate, and bandwidth exceeding 10 GHz are generated at both integer and fractional Talbot conditions. At detuned Talbot conditions pulses are shown to be tailorable by recirculation-induced first-order dispersion. The far-field character of the resulting waveforms is demonstrated, and the performance in terms of amplitude noise and timing jitter, in this last case after the introduction of active loop stabilization, is evaluated.

1. Introduction

The generation of optical pulses with prescribed temporal or spectral phase characteristics is of significant importance in both the fundamental and applied domains. Phase-coded, stepped frequency, or linearly chirped pulses, for instance, are employed in a variety of fields such as reflectometry, optical fiber sensors, real-time signal processing, lidar, and photonics-assisted radar. Nonlinearly chirped pulses also have a wide range of applications. Nonlinear frequency-to-time maps have been used to generate tunable linear frequency-modulated electrical waveforms [1, 2, 3, 4]. Real-time acquisition systems benefit from nonlinear characteristics to provide significant savings in storage requirements [5, 6, 7] and, using similar principles, nonlinearly chirped waves have been used for multiscale time-frequency analysis of microwave signals [8]. Also, photonics-assisted generation of nonlinear frequency-modulated continuous waves designed to decrease the correlation peak-to-sidelobe ratio of broadband radar signals have been demonstrated [9]. In a broader context, optical pulses with general spectral phase profiles attract continuous attention due to its unique linear [10, 11] and nonlinear [12] propagation properties, and temporal or spectral pulse engineering can be combined with spatial beam conformation to generate spatio-temporal wavepackets with unconventional behavior under both dispersion and diffraction [13, 14, 15].

High-order dispersive propagation represents one of the most successful approaches for the generation of nonlinearly chirped pulses, either as a perturbation of a linear chirp [1, 2, 3] or in the far field, where dispersion is dominant [5, 10]. If a transform-limited optical pulse of

spectral width σ_ω propagates in a medium with spectral phase characteristics relative to the carrier ω_0 given by $\Phi(\omega) = \beta_m(\omega - \omega_0)^m/m!$, where β_m is the dispersion coefficient with m integer ≥ 2, the corresponding higher-order Fraunhofer domain can be defined as the region where $|\beta_m|\sigma_\omega^m/m! \gg \pi$. In this regime, the stationary phase approximation [16] describes a pulse whose instantaneous frequency follows a frequency-to-time law of the form $\omega^{m-1} \propto t$ or, equivalently, a pulse whose temporal phase is $\propto t^{m/(m-1)}$. These scaling laws generalize those of linearly chirped pulses generated by first-order dispersion (β_2), which are recovered for $m = 2$.

Airy pulses represent the following example of this family, which are generated in the far field of second-order dispersion (β_3) where the dominant spectral phase is cubic ($m = 3$). Introduced by Berry and Balazs within the context of quantum mechanics [17], Airy wavepackets are characterized by a probability density whose free propagation is distortionless and self-accelerates as a classical particle subject to a constant force. However, as the probability density is non-integrable, the optical generation of Airy waves takes on the form of finite-energy Airy beams or pulses that nonetheless maintain these characteristic features [18, 19]. This family of waves have captured considerable attention as they show additional properties, such as self-healing [20] or several effects in Kerr media: soliton shedding [21, 22], tight focusing and asymmetric inversion [23, 24], nonlinear spectral reshaping [25], and particular forms of Airy-soliton interaction [26], to name a few. The generation of Airy pulses, and also of higher-order far-field pulses [10] and fractional generalizations [11], usually relies on the phase filtering of the spectrum of a mode-locked laser by a programmable spectral filter [22, 25] or a grating-telescope compressor [13, 14]. In addition, Airy pulses are also generated in standard telecom fiber at data rates in excess of 100 Gb/s [27]. These approaches, however, suffer from the unavoidable losses associated to external filtering or fiber propagation and are restricted to ultrashort pulses (from sub-ps to fs) as their broadband spectrum allows to reach the Fraunhofer regime at moderate values of second-order dispersion.

In this paper we present an alternative method for the generation of Airy pulses at the ns pulse width scale. It is based on the design of a Talbot laser that creates an optical frequency comb where the different spectral lines acquire large cubic spectral phases upon multiple recirculations in a dispersive laser cavity incorporating a frequency shifter. This approach, which can be generalized to more general families of pulses with other temporal and spectral characteristics, represents, to the best of our knowledge, the first laser system that directly generates this type of pulses.

A Talbot laser is an injection-seeded active cavity that incorporates a frequency shifting element, and so its output is built on the coherent addition of recirculating and frequency-shifted waves [28, 29, 30, 31]. We restrict the name of Talbot laser to injection-seeded active cavities operating above threshold; when operated below threshold they will be referred to as frequency-shifting loops. Unseeded frequency-shifting active cavities are conventionally designated as frequency-shifted feedback lasers [32]. Both Talbot lasers and frequency shifting loops offer a generic advantage in terms of bandwidth, as they generate multi-GHz frequency combs, eventually in the form of pulse trains, from low-frequency electronics [33]. Benefiting from standard telecom technology, they have found a broad range of applications.

Restricting the account to pulse or waveform generation methods, they have been used for generating stepped-frequency optical and radio-frequency (RF) signals [34, 35, 36] for spectroscopy [37, 38] and radar [39, 40, 41, 42], transform-limited pulses [28, 31, 43, 44, 45], and also linearly [33, 39] and nonlinearly [46, 47] chirped pulses, in this last case after the introduction of an intracavity phase modulator. In the present context, the distinctive feature of cavities incorporating a frequency shifter is that the recirculation of a monochromatic wave under dispersion of order m generates optical pulses which present an effective dispersion of increased order $m+1$. The simplest example of this property is the recirculation of an optical wave in a dispersion-free cavity, which generates far-field linearly chirped pulses [33, 48].

Our system extends this approach using a first-order ($m = 2$) highly dispersive fiber ring cavity incorporating an acousto-optic frequency shifter (AOFS) and an EDFA as gain element. Dispersion is introduced by linearly chirped fiber Bragg gratings (LCFBG), and finite-energy Airy pulses are generated through spectral truncation, namely, a limitation in the number of recirculations imposed by the LCFBG. These waveforms constitute a family of bandlimited, single-sided far-field Airy pulse trains with repetition rates in the 80-MHz range that can reach sub-ns pulse widths. The waveforms are tunable though the shifting frequency, which introduces a controlled amount of effective first-order dispersion in the pulse spectrum. The resulting family of bandlimited pulses is shown to be described by a previously developed theory [49], which is here confirmed for the first time. The far-field character of the generated Airy pulses is experimentally verified. Recirculating ASE, which represents a major noise source in Talbot lasers [31, 44, 50, 51], is controlled by a suitable choice of the injection wavelength within the LCFBG reflection band. Specific tests of amplitude and timing stability, in this last case after the introduction of active loop control, were conducted to assess the feasibility of the approach.

The paper is organized as follows. In Section 2 we explain the principle of operation and derive the associated far-field condition. Section 3 describes the experimental setup and the laser operation regime. Section 4 introduces the analytic model accounting for the pulses at and near Talbot conditions, and Section 5 analyzes the obtained bandwidth, the induced cubic spectral phases, and the different waveforms generated together with a specific study of time and amplitude stability. Finally, we end in Section 6 with our conclusions.

2. Principle of operation

Airy pulses are defined by the presence of a dominant cubic spectral phase in its Fourier transform. This type of pulses can be generated in a dispersive frequency-shifting ring cavity as follows. Let us consider the recirculation of a monochromatic wave in such a cavity, schematically depicted in Fig. 1(a) in its fiber version. In the frequency shifter (FS), the recirculating wave is shifted by an angular frequency $\Omega_s = 2\pi f_s$ equal to the RF sinusoidal drive signal. Roundtrip losses, partially compensated by the amplifier (G) and controlled by the RF power delivered to the FS, are assumed constant in the band of interest. They will be described by an amplitude attenuation factor $\rho \lesssim 1$, so that the cavity is assumed to operate below threshold, as a frequency-shifting loop.

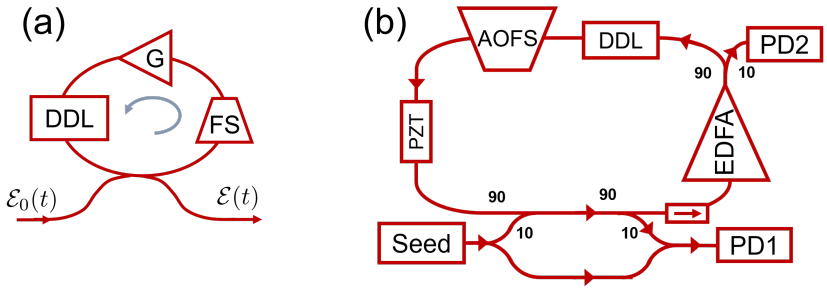

Figure 1. (a) Scheme of an amplified dispersive frequency-shifting ring cavity. (b) Scheme of the experimental setup.

The single-pass propagation characteristics are lumped into an equivalent dispersive delay line (DDL) described by the spectral phase term $\exp(-j\Phi(\omega))$ acquired by an optical frequency ω. Under the standard narrowband assumption, the spectral phase is expressed as:

$$\Phi(\omega) = \omega_0\tau_p + (\omega-\omega_0)\tau_g + \frac{1}{2}\varphi(\omega-\omega_0)^2 \tag{1}$$

Here, ω_0 is a reference frequency, τ_p and τ_g are, respectively, phase and group delays, and φ is the (first-order) dispersion coefficient, all of them evaluated at frequency ω_0.

If we seed the cavity with a monochromatic wave at the reference frequency, $\mathscr{E}_0(t) = E_0 e^{j\omega_0 t}$, the output field $\mathscr{E}(t)$ is created by the coherent addition of frequency-shifted replicas of the input, and results is a single-sided frequency comb with spectral separation Ω_s:

$$\mathscr{E}(t) = E_0 e^{j\omega_0 t}\sum_{n=0}^{\infty}\rho^n e^{-j\phi_n}e^{jn\Omega_s t} \tag{2}$$

The phase ϕ_n of the n-th spectral line is the accumulated spectral phase after n roundtrips, which is augmented in each recirculation by the single-pass spectral phase at frequency $\omega_0 + n\Omega_s$. This results in a recurrence that represents a discrete or finite-time integrator seeded with the DDL characteristics:

$$\phi_n = \phi_{n-1} + \Phi(\omega_0 + n\Omega_s) \tag{3}$$

where $n \geq 0$ stands for the number of roundtrips or frequency shifts undergone by the seed frequency. When the dispersive phase is purely of order m, this recurrence is solved in terms of Bernoulli polynomials [52] of order $m+1$ in the running variable n. In our case, the recurrence for the DDL (1) is:

$$\phi_n = \phi_{n-1} + \omega_0\tau_p + \Omega_s\tau_g n + \frac{1}{2}\varphi\Omega_s^2 n^2 \qquad \phi_0 = 0 \tag{4}$$

with solution:

$$\phi_n = n\omega_0\tau_p + \frac{1}{2}n(n+1)\Omega_s\tau_g + \frac{1}{12}n(n+1)(2n+1)\varphi\Omega_s^2 \tag{5}$$

In our experiment, we can neglect $|\varphi|\Omega_s$ against τ_g, see Section 3, so the spectral phases of the comb lines simplify to:

$$\phi_n = n\omega_0\tau_p + \frac{1}{2}n(n+1)\Omega_s\tau_g + \frac{1}{6}n^3\varphi\Omega_s^2 \tag{6}$$

The spectral phases of the output comb present a cubic dependence in the line index n, which represents an effective second-order dispersion induced by the recirculation of the seed in the first-order dispersive frequency-shifting loop. The generation of cubic spectral phases is thus a linear process. Effective dispersion coefficients β_k ($k = 1,2,3$) can be read from this expression by equating it to a polynomial expansion $\phi_n = \sum_{k=1}^{3}\beta_k(n\Omega_s)^k/k!$. The group delay β_1 is linear in the input frequency, $\beta_1 = \omega_0\tau_p/\Omega_s + \tau_g/2$. The accumulated first and second-order dispersion coefficients are respectively given by $\beta_2 = \tau_g/\Omega_s$ and $\beta_3 = \varphi/\Omega_s$. Note that the effective second-order dispersion β_3 is induced by recirculation in a DDL characterized by φ in the same manner that β_2 is induced by τ_g [33].

As will be analyzed with more detail in Section 4, the second term in (6) provides an integer number of cycles at the so-called integer Talbot conditions, where $\Omega_s\tau_g = 2\pi p$ with p an arbitrary positive integer. Under this condition, the phases ϕ_n only contain a delay and a cubic phase and therefore the comb appears as a train of Airy pulses with repetition rate Ω_s. If we denote by N the number of recirculating spectral lines, eventually determined by a spectral filter, the comb's spectral width is $N\Omega_s$ and so the far-field condition is given by $N^3|\varphi|\Omega_s^2 \gg 6\pi$.

3. Experimental system

3.1. Experimental setup

The scheme of the experiment, depicted in Fig. 1(b), is based on a previously reported frequency-shifted feedback laser [53]. The fiber loop is composed of a home-made EDFA comprising 60 cm of highly-doped fiber (Liekki Er80/8) pumped at 980 nm, operated at a fixed gain of 19 dB and with saturation power of 20 mW and noise figure < 4.5 dB. It is followed by a DDL implemented by three LCFBG (Teraxion), placed in tandem using circulators. Each LCFBG has a nominal dispersion of 600 ps/nm in a flat 0.8-nm band around 1.55 μm. The nominal DDL dispersion parameter is thus $\varphi = -2300$ ps^2/rad, and the recirculation-induced second order dispersion $\beta_3 = \varphi/\Omega_s$ as large as -4.58×10^6 ps^3/rad^2 at $\Omega_s/2\pi = 80$ MHz. The far field condition $N^3|\varphi|\Omega_s^2 \gg 6\pi$ is reached when the optical comb comprises $N > 70$ spectral lines.

The loop includes a fiber-coupled AOFS (AA Opto) providing positive frequency shifts around 80 MHz, a PZT fiber stretcher (Idil Fibres Optiques) for active stabilization, filter couplers for power injection and extraction, and an isolator to assure unidirectional recirculation. The system was based on polarization-maintaining components, except the EDFA, after which a polarization controller (not shown in the figure) was placed to align the recirculating state of polarization.

We provided external injection (Seed) using a tunable single-wavelength fiber laser at $\sim$ 1550 nm (NKT Koheras E15) with linewidth < 100 Hz. An additional fiber path was included for heterodyne measurements of the optical field using a 40-GHz photodiode (PD1) followed by a real time oscilloscope (RTO) of 6-GHz bandwidth (LeCroy SDA 6000A). We also injected a second out-of-band, and thus non-recirculating, wavelength at 1562.80 nm, not shown in the figure, to monitor in real time the EDFA gain and compression levels at the low-bandwidth photodiode PD2 [53]. The characterization was completed by standard spectral and intensity measurements. Active stabilization was provided from an error signal obtained by tapping the intracavity field after the EDFA and mixing the intensity detected at PD2 with the RF driving frequency Ω_s followed by electrical lowpass filtering. Stabilization is provided in a 10-kHz bandwidth by an analog PID controller (SRS SIM960) acting on the PZT actuator.

Single-roundtrip losses were controlled by the RF power delivered to the FS and attained -15 dB at the maximum rated power. Different cavities were used in the experiments. The corresponding roundtrip group delays, with magnitude $\sim$ 200 ns, were determined in each case by the shifting frequencies Ω_s that lead to integer and fractional Talbot conditions at 1550 nm. The output power was below the milliwatt (-6 dBm), as is typical in this type of configurations [31, 33].

3.2. Injection wavelength

Both in Talbot lasers and in frequency-shifting loops the recirculation of the coherent seed competes with ASE for the same gain [32]. ASE recirculation is manifested in a non-white noise background that repeats quasiperiodically at a rate equal to the FSR [44, 51, 53]. At high noise levels, ASE can drive the relaxation oscillations of the amplified loop, leading to large envelope variations consequence of gain fluctuations [53]. Specific noise-suppression techniques, such as intracavity filters [33] or loss modulation [31], are usually employed to reduce the level of ASE recirculation. In our experiment we optimized the emission by operating the laser in the main spectral net gain region, so that the external injection in this band picks up most of the gain at the expense of ASE [28]. To explain the procedure, we performed an specific experiment using a short cavity (without the PZT element) with $\tau_g = 178.2$ ns (FSR = 5.612 MHz).

In Fig. 2(a) we show, with blue and magenta traces, two regimes of the laser emission spectrum when the active fiber ring is not seeded. In blue, the unseeded laser is $\sim$ 1 dB below threshold and its spectrum follows the approximately flat-top 0.8-nm LCFBG reflection band. As the ASE recirculation is damped below threshold, this curve is representative of the actual shape of the gain spectrum. In magenta we plot the emission spectrum when the unseeded laser is above threshold at a gain compression of $\sim$ 1.5 dB, where the laser is Q-switched (QS) by self-sustained relaxation oscillations [53]. The spectrum has a main peak at the low-wavelength end, with ripples caused by the $\sim$5 kHz QS pulse train. The spectrum also shows a secondary peak near the center of the band. The two peaks are due to the accumulation of ASE that undergoes amplification while being frequency shifted towards lower wavelengths

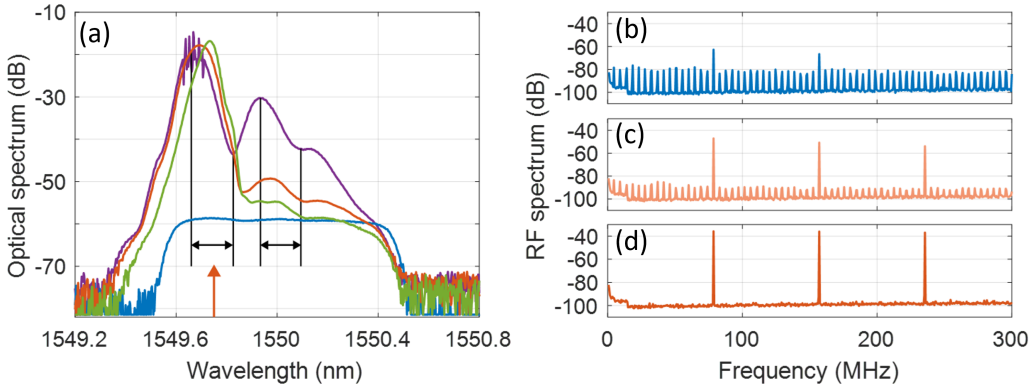

Figure 2. (a) Laser emission spectrum under different operation conditions: blue, without external injection and $\sim$ 1 dB below threshold; magenta, without external injection and above threshold at a compression level of $\sim$ 1.5 dB; orange, injected at 1549.75 nm with power 2 μW; green, injected with power 8 μW. The horizontal arrows mark the two spectral net gain regions of the cavity, and the vertical arrow the seed wavelength. (b)-(d) RF spectrum of the intensity for the (b) unseeded cavity, and injected at 1550.16 nm with (c) 0.5 μW and (d) 3 μW. Resolution bandwidth, 1 kHz.

[54]. Spectral peaks and valleys locate the wavelengths for which the cavity is at threshold and where the process of amplified ASE recirculation begins (valleys) or ceases (peaks). From this observation, the spectral net gain regions can be graphically estimated, as is also shown in the figure, and correspond to the local maxima of the LCFBG amplitude ripples.

The seed wavelength where injection competes more effectively with ASE is thus that in the beginning of the main net gain region in the opposite direction of the frequency shift, here at $\simeq$ 1549.75 nm. As we increase the injection power, the EDFA compression is initially kept invariant. In this regime the total recirculating power (ASE + seed) remains constant in a homogeneously broadened amplifier, so that an increase in injection is accompanied by a reduction of ASE power. In Fig. 2(a) we show, in orange, the spectrum when the power of the optimal seed wavelength is 2 μW. This is the maximum injection power that keeps the initial compression level of $\sim$ 1.5 dB, so the initial ASE power is maximally substituted by the seed. The decrease in ASE power is clearly visible in the 20-dB reduction of the high-wavelength peak in the secondary gain region. This secondary peak can be even vanished under a higher level of injection, which increases compression and drives the secondary peak below threshold, as is shown in Fig. 2(a) with a green trace.

We also point out that the relative amplitude of the spectral gain regions could be slightly tuned through the polarization controller placed after the EDFA, a fact that we ascribe to polarization-dependent loss in the LCFBG. This way, the roles of main an secondary gain regions could be interchanged. In a second experiment, we observed the effect of ASE substitution in the RF intensity spectrum of a longer cavity operated in the high-wavelength gain region at the $p = 17$ Talbot condition. As is shown in Fig. 2(b), the intensity spectrum of the unseeded laser shows ASE resonances separated by an FSR $= 4.620$ MHz. The 17th and 34th resonances, which coincide with the shifting frequency and its second harmonic, are here

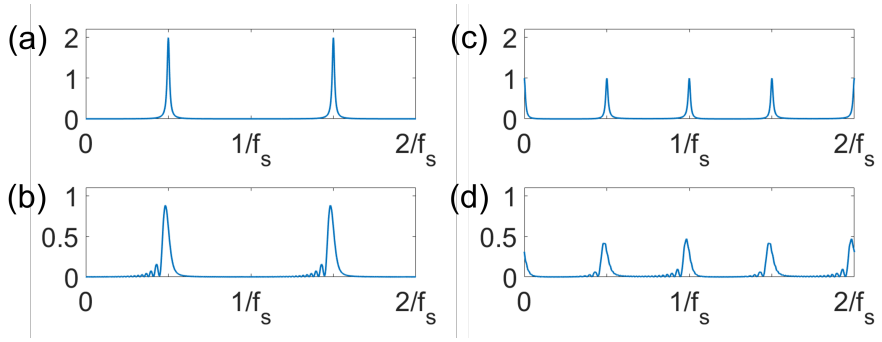

Figure 3. Simulated intensity traces of Talbot lasers at integer Talbot condition without (a) and with (b) intracavity dispersion, and at semi-integer Talbot condition without (c) and with (d) dispersion. In (c) and (d) the intensities show a twofold increase in pulse repetition rate.

reinforced due a residual modulation in the AOFS [44, 53, 55]. With progressive injection of seed power, which appears at the repetition rate $f_s = 17 \cdot \mathrm{FSR}$ and its harmonics, the ASE bands are clearly reduced, as is shown in Fig. 2(c) and (d).

4. Bandlimited Airy pulses

4.1. Airy pulses at Talbot conditions

The use of model (2) for the description of the laser output deserves some justification. Following a previous analysis [32], we first observe that the seed wavelength recirculates in the spectral net gain region a finite number of roundtrips, say N. Each spectral line shows an accumulated amplitude gain μ_n equal to the product of amplitude gain factors accumulated after the n recirculations. This factor, which substitutes for ρ^n in (2), can be approximately flat ($\mu_n \simeq$ const.) or gaussian-shaped, depending on the curvature of the gain region [32]. If the injection level is so high that it drives the gain region below threshold, the recirculating seed undergoes recurrent attenuation and (2) is valid with $\rho < 1$. Thus, (2) can be applied above threshold for the analysis of flat or exponentially decaying combs provided we introduce the appropriate spectral cutoff associated to the finite number of recirculations $n \leq N$.

In the analysis of (2) it is convenient to define a periodic envelope that is temporally shifted by the wavelength-dependent delay, $\overline{\tau} = \omega_0 \tau_p / \Omega_s$, of the group delay β_1. The electric field is thus presented as $\mathscr{E}(t) = E(t-\overline{\tau})e^{j\omega_0 t}$ where, using (6), the optical envelope is:

$$E(t) = E_0 \sum_{n=0}^{\infty} \rho^n e^{-j\frac{1}{2}\Omega_s \tau_g n(n+1) - j\frac{1}{6}\varphi\Omega_s^2 n^3 + jn\Omega_s t} \tag{7}$$

The different types of waveforms with regard to Talbot effect can be described as follows. Let us first consider a situation where the frequency shift is tuned to an integer multiple of the FSR, $\Omega_s \tau_g = 2\pi p$ with p a positive integer, so that the first phase term in (7) equals unity. As this phase term is quadratic in the spectral line index n, this situation can be interpreted as providing an integer Talbot replica of a pulse train. If, in addition, the intra-loop dispersion is absent, $\varphi = 0$, (7) describes a pulse train with exponentially decaying spectrum, and so

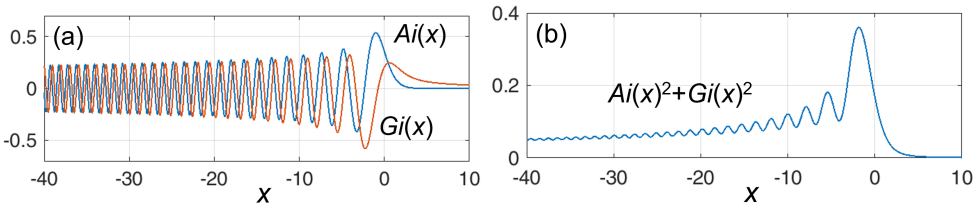

Figure 4. (a) Airy $\mathrm{Ai}(x)$ (blue) and Scorer $\mathrm{Gi}(x)$ (orange) functions. (b) Intensity of the single-sided Airy wave $\mathrm{Ai}(x) + j\,\mathrm{Gi}(x)$.

with Lorentzian intensity, at a repetition rate equal to the frequency shift. This situation is schematically depicted in Fig. 3(a). In the general case where $\varphi \neq 0$, the periodic envelope can be expressed as a succession of pulses $p(t)$ as $E(t) = \sum_k p(t - k/f_s)$, with:

$$p(t) = E_0 \int_0^\infty \frac{d\omega}{\Omega_s} e^{-\varepsilon\omega} \exp\left(-j\frac{\varphi}{6\Omega_s}\omega^3 + j\omega t\right) \tag{8}$$

and where we have written $\rho = \exp(-\varepsilon\Omega_s)$ with $\varepsilon \gtrsim 0$ the exponential decay factor per unit shifting frequency. In our experiment $\varphi < 0$, and so the real part or in-phase component of $p(t)$ is, up to scale factors and in the limit $\varepsilon \to 0$, the standard Airy function

$$\mathrm{Ai}(x) = \int_0^\infty \frac{du}{\pi} \cos\left(\frac{1}{3}u^3 + ux\right) \tag{9}$$

Conversely, the imaginary part or quadrature component of (8) becomes the inhomogeneous Airy or Scorer function $\mathrm{Gi}(x)$ [52]. These in-phase and quadrature components, together with the intensity, are depicted in Figs. 4(a) and (b), respectively. Due to the presence of the slowly-decaying tails and in the absence of any frequency cutoff, they carry infinite energy. The truncation necessary for rendering an Airy pulse of finite energy is implemented in (8) through the spectral decay parameter ε. In our experiment, however, the spectral truncation is obtained by bandlimiting the wave's spectrum so, as pointed out before, frequency combs with both decaying ($\varepsilon > 0$) and flat spectra ($\varepsilon \simeq 0$) can be generated in limited bandwidths by controlling the loop's loss.

Asymptotic analysis [16] of (8) provides convenient analytic approximates to the Airy pulse in the far field. The stationary phase condition defines an instantaneous frequency $\omega_i(t)$ for each negative time t, following the parabola $\omega_i(t) = \kappa\sqrt{-t}$ and with a scale factor:

$$\kappa = \sqrt{\frac{2\Omega_s}{|\varphi|}} \tag{10}$$

The inverse equation, $t_i(\omega) = -\omega^2/\kappa^2$, represents the nonlinear frequency-to-time map that assigns spectral components to temporal instants in the range $t < 0$. The stationary phase approximation results in the following asymptotic description of the pulse for $t < 0$:

$$p(t) = \frac{E_0 e^{-\varepsilon\kappa\sqrt{-t}}}{[2\pi f_s^3 |\varphi| (-t)]^{\frac{1}{4}}} \exp\left(-j\frac{2}{3}\kappa(-t)^{3/2} + j\frac{\pi}{4}\right) \tag{11}$$

whereas the behavior for $t > 0$ is exponentially small. With our design values the scale factor is $\kappa = 20.9$ rad/ns$^{3/2}$, and so the typical temporal scale of phase variations lies in the ns range. The pulse width, which also lies in this range, is thus lower than the train's period $1/f_s \sim 12.5$ ns and can be controlled through the amplitude decay factor ε. The output comb appears as a train of Airy pulses, as exemplified in Fig. 3(b).

This description can be generalized to fractional Talbot conditions, which are defined by the requirement $\Omega_s \tau_g = 2\pi \times p/q$ with p and q coprime and positive integers. According to the general theory [56], the output field is periodic with the same repetition rate Ω_s, and in the time domain each fundamental period is composed of q replicas of the basic pulse $p(t)$ mutually shifted by $1/qf_s$ and with relative phase factors following a Gauss phase sequence of length q [57, 58, 48]. The repetition rate of the intensity is thus multiplied by a factor of q, and the energy distributed in q equal pulses per period. This situation is exemplified in Figs. 3(c) and (d) for Lorentzian ($\varphi = 0$) and Airy pulses ($\varphi \neq 0$), respectively, for a semi-integer Talbot condition.

4.2. Airy pulses at detuned Talbot conditions

In a similar manner as in a dispersion-free frequency shifting fiber loop [33], a small detuning of the shifting frequency from (integer or fractional) Talbot conditions leads to the effective induction of first-order dispersion in the pulse $p(t)$. Let us consider a shifting frequency given by $\Omega_s = \overline{\Omega}_s + \Delta\Omega_s$, where $\overline{\Omega}_s$ is tuned to an integer Talbot condition and $\Delta\Omega_s \ll \overline{\Omega}_s$. Using this decomposition in the first phase term of (7) we are led to:

$$E(t) = E_0 \sum_{n=0}^{\infty} \rho^n e^{-j\frac{1}{2}\Delta\Omega_s \tau_g n(n+1) - j\frac{1}{6}\varphi\Omega_s^2 n^3 + jn\Omega_s t} \tag{12}$$

A temporal shift $\tau_g \Delta\Omega_s/2\Omega_s$ is induced in the envelope, which can be a delay or an advance depending on the sign of $\Delta\Omega_s$, plus a quadratic spectral phase that is equivalent to first-order dispersion. Neglecting the temporal shift, the envelope can be presented as a train of pulses of the form:

$$p(t) = E_0 \int_0^{\infty} \frac{d\omega}{\Omega_s} e^{-\varepsilon\omega} \exp\left(-j\frac{\tau_g \Delta\Omega_s}{2\Omega_s^2}\omega^2 - j\frac{\varphi}{6\Omega_s}\omega^3 + j\omega t\right) \tag{13}$$

The induced first-order dispersion $\tau_g \Delta\Omega_s/\Omega_s^2$ is normal (anomalous) for positive (negative) values of $\Delta\Omega_s$, and can also attain large values: with $f_s = 80$ MHz and $\tau_g = 200$ ns this factor is ~ 5000 ps^2/rad per kHz of detuning, equivalent to the dispersion of $\sim$250 km of standard telecom fiber in the C band.

The family of envelopes (13) can be analyzed from its time-frequency representation [49]. As is immediate to show, the stationary phase condition defines an instantaneous frequency that follows a shifted parabola in the $t - \omega_i$ plane,

$$\kappa^2(\Delta t - t) = (\omega_i(t) - \Delta\omega)^2 \tag{14}$$

where the spectral and temporal shifts are given by:

$$\Delta\omega = -\frac{\tau_g \Delta\Omega_s}{\varphi\Omega_s} \qquad \Delta t = \frac{\Delta\omega^2}{\kappa^2} \tag{15}$$

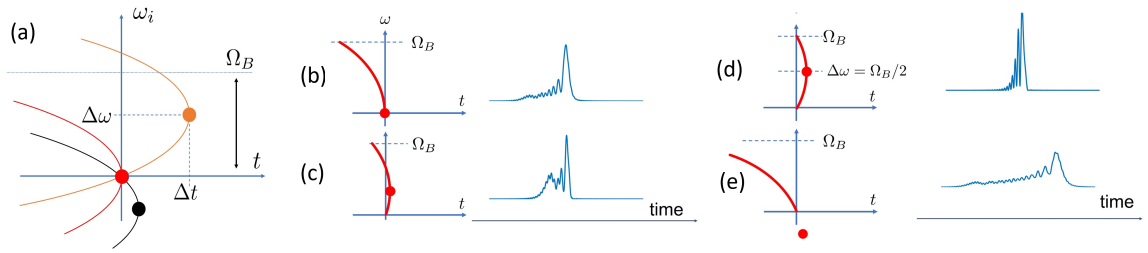

Figure 5. (a) Time-frequency representation of the bandlimited Airy pulses. The parabolas correspond to $\Delta\omega = 0$ (red), $\Delta\omega > 0$ (orange), and $\Delta\omega < 0$ (black), with their vertices highlighted with dots. (b)-(e) Schematic parabola (left) and simulations of the intensity (right) of Airy pulses for different values of the spectral shift $\Delta\omega$. Plots (b) and (d) describe, respectively, the single-sided and the double-sided Airy pulses used as references.

With our design values, the $\Delta\omega/\Delta\Omega_s$ factor is 172 MHz/kHz, and so a detuning by a few kHz shifts the parabola in time and frequency in ns and GHz ranges, respectively. In the absence of detuning-induced dispersion ($\Delta\omega = \Delta t = 0$) we recover the previous parabola $\omega_i(t) = \kappa\sqrt{-t}$ whose vertex lies in the origin of the time-frequency plane, as is schematically shown with a red trace in Fig. 5(a). In general, the temporal shift is always positive but the spectral shift can be positive or negative depending on the signs of $\Delta\Omega_s$ and φ. This moves the vertex of the parabola in the first or fourth quadrants of the $t - \omega_i$ plane. However, and due to the second relationship in (15), the origin of the plane $\omega_i = t = 0$ lies in any parabola obtained by detuning. The possible situations (zero, positive or negative $\Delta\omega$) are schematically depicted in Fig. 5(a).

4.3. Bandwidth limitation

The spectrum of the Airy pulses is contained in the range $\omega_i \geq 0$, as the integral representation (13) does not involve negative frequencies. If, in addition, the pulse is bandlimited, the integral is cutoff by a bandwidth Ω_B. In the experiment, this bandwidth is provided by the extent of the spectral gain band used for pulse generation, typically about 10 GHz. In heterodyne measurements, Ω_B is explicitly dictated by the RTO electrical detection bandwidth (6 GHz).

In either case, bandlimited Airy pulses are described by a strip $0 \leq \omega_i \leq \Omega_B$ in the time-frequency plane. From this observation it can be provided a qualitative description of the pulse intensity [49]. The single-sided Airy pulse, simulated in Fig. 5(b), is taken as our default situation. When the spectral shift $\Delta\omega$ lies in the strip $0 \leq \Delta\omega \leq \Omega_B$, the vertex of the parabola represents the spectral content of the pulse's trailing edge, where a number of frequency components accumulate in approximately the same time. This leads to a wavy 'head' [49] in the trailing edge composed of peaks with increasing heights, produced by the interference of the symmetrically distributed frequencies around the vertex. This head is preceded by a smooth 'tail' due to the mismatched, temporally spread frequencies. This structure is exemplified in Fig. 5(c).

The main peak of the head becomes the shortest and the tail is absent at $\Delta\omega = \Omega_B/2$,

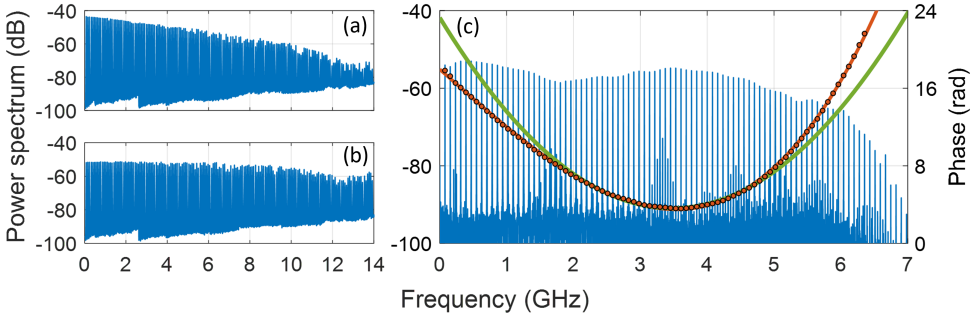

Figure 6. Heterodyne power spectrum for an (a) exponentially decaying and a (b) flat comb, measured in a RF spectrum analyzer (resolution bandwidth, 1 kHz). (c) Heterodyne FFT power spectrum (blue, left scale) and phase of the spectral lines (orange dots, right scale) measured from a digitized temporal trace (measurement time, 3.2 µs; spectral resolution, 275 kHz). The fitted cubic phase is shown with a continuous orange trace. The green trace is a parabolic fit of the phase minimum plotted to ease the visualization of the positive cubic component. The noise level in (c) corresponds to ADC noise plus spurious tones of electronic origin.

see Fig. 5(d), as all the frequencies are approximately grouped at the same instant in the time-frequency plane. The structure of this envelope can be described as follows: shifting the integration variable in (13) as $\omega = \omega' + \Delta\omega$ and making use of (15), we find:

$$p(t) = E_0 e^{-\varepsilon\Delta\omega} e^{j\Delta\omega(t-\frac{2}{3}\Delta t)} \tag{16}$$
$$\times \int_{-\Delta\omega}^{\Omega_B-\Delta\omega} \frac{d\omega'}{\Omega_s} e^{-\varepsilon\omega'} \exp\left(-j\frac{\varphi}{6\Omega_s}\omega'^3 + j\omega'(t-\Delta t)\right)$$

When $\Delta\omega = \Omega_B/2$ and assuming a flat comb ($\varepsilon = 0$) the pulse envelope reads

$$p(t) = E_0 e^{j\frac{\Omega_B}{2}(t-\frac{2}{3}\Delta t)} \tag{17}$$
$$\times \int_{-\frac{\Omega_B}{2}}^{\frac{\Omega_B}{2}} \frac{d\omega'}{\Omega_s} \exp\left(-j\frac{\varphi}{6\Omega_s}\omega'^3 + j\omega'(t-\Delta t)\right)$$

The envelope is thus carried at a frequency $\Omega_B/2$, and its amplitude is real and equals an Airy function of the type (9), but bandlimited to $\Omega_B/2$. This envelope will be referred as the two-sided Airy envelope and, together with the bandlimited single-sided pulse shown in Fig. 5(b) represent the two reference fields in our analysis. In the rest of the situations, when the frequency shift $\Delta\omega$ is negative or exceeds the bandwidth Ω_B, the high frequencies are located in the leading or trailing edges, respectively, following the nonlinear frequency to time map described by parabola (14). In these cases, the intensity appears stretched toward these high frequencies and does not show sharp peaks. This is exemplified for $\Delta\omega < 0$ in Fig. 5(e), where the pulse appears stretched to the leading edge.

5. Results

5.1. Bandwidth and spectral phase

To explore the actual laser performance, the system was configured in the complete setup described in Fig. 1(b). The cavity was operated at the central gain peak in Fig. 2(a). This

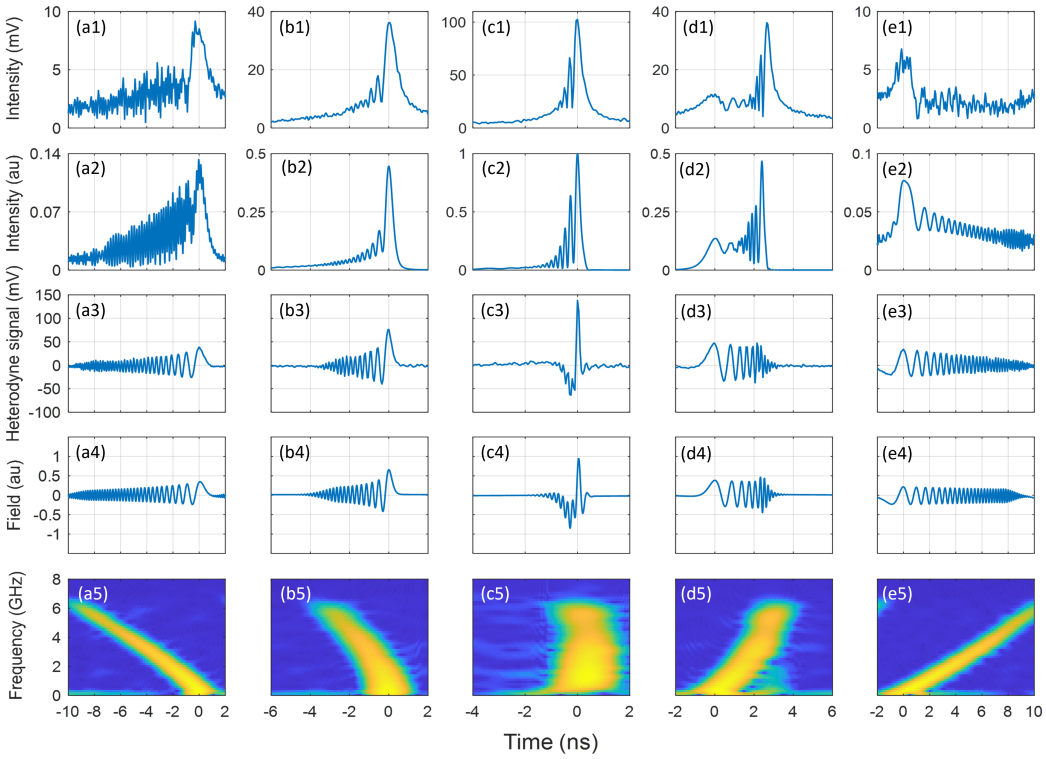

Figure 7. Intensity (1, top row), simulation of the intensity (2, second row), heterodyne signals (3, third row), simulated in-phase components of the field (4, fourth row) and spectrograms of the heterodyne signal (5, bottom row) corresponding to different bandlimited Airy pulses generated by detuning the frequency shift from the $p = 17$ Talbot condition. Columns correspond to detuned frequencies $\Delta\Omega_s/2\pi$ equal to (a) -32 kHz, (b) 0 kHz ($p = 17$ Talbot), (c) 16 kHz, (d) 32 kHz, and (e) 64 kHz.

wavelength was chosen to use the central part of the LCFBG reflection spectrum, thus avoiding the use of the low-wavelength end that corresponds to the input port of the flat-topped LCFBGs where the impact group delay ripples is more detrimental [59, 60]. The laser was operated with an injection wavelength of 1550.16 nm, at typical compression levels of $1.5-2$ dB, and with frequency shifts at or near the $p = 17$ integer Talbot condition. At this wavelength, the cavity has a roundtrip group delay $\tau_g = 215.9$ ns (FSR $= 4.632$ MHz). The laser could be adjusted through the injection level to provide exponentially decaying and flat combs in ~ 10 GHz bandwidths ($N \sim 125$ spectral lines), as determined by wideband RF spectral measurement of the heterodyne signal, see Fig. 6(a) and (b).

We performed a specific experiment to check the induction of cubic spectral phases by the dispersive cavity. An heterodyne trace was taken at $f_s = 78.744$ MHz, which nominally corresponds to the $p = 17$ Talbot condition. At this point, the spectral phase is ideally cubic, although even a small mismatch of a fraction of kHz induces an unavoidable quadratic component. The heterodyne signal was Fourier transformed to acquire amplitude and phase of the optical spectral lines above the injected carrier, plotted in Fig. 6(c). We introduced a numerical delay in the spectral phase (i.e., a linear phase term) to place the minimum of the phase at the center of the band, as so ease the visualization of the cubic contribution. A fit

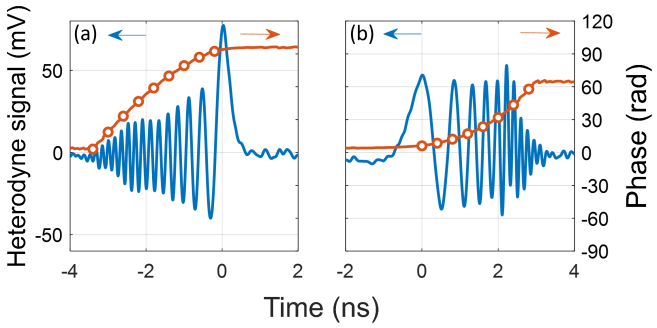

Figure 8. (a) Blue trace (left scale): heterodyne signal of the single-sided Airy pulse. Orange trace (right scale): temporal phase extracted after Hilbert transform. Orange points (right scale): temporal phase fitted to a $(-t)^{3/2}$ law. (b) Same as (a) for the Airy pulse with $\Delta\omega = \Omega_B$.

provides a value of this cubic term of 0.170 rad/GHz^3, to be compared with the nominal value 0.189 rad/GHz^3 given by (6). In repeated tests with different values of Ω_s we found consistent values of the cubic term, differing at most 15% with respect to this nominal value.

5.2. Waveforms

We also conducted some experiment to explore the different waveforms generated by the laser. The results, presented in Fig. 7, are organized in columns corresponding to Airy pulses with different amounts of first-order dispersion induced by detuning the shifting frequency. The single-sided Airy pulse obtained at the integer Talbot condition, shown in column (b), represents the default situation. Following the time-frequency representation of Fig. 5, the rest of the columns can be characterized by the vertex of the parabola: (a) an Airy pulse with negative frequency shift $\Delta\omega$ and thus highly stretched towards the leading edge, (c) an Airy pulse with positive $\Delta\omega$ equal to half the detection bandwidth, corresponding to the double-sided Airy pulse described in (17), (d) an Airy pulse with positive $\Delta\omega$ equal to the detection bandwidth, and finally (e) an Airy pulse with positive $\Delta\omega$ beyond the detection bandwidth and thus highly stretched towards the trailing edge.

For each of these five situations we provide in row 1 single-shot traces of the intensity, in row 3 the corresponding heterodyne signal, and in row 5 the spectrogram of the heterodyne signal. In rows 2 and 4 we plot, respectively, simulations of the intensity and in-phase component of the field. These simulations are based on (12) with $\rho = 0.95$, taking into account the 6-GHz bandwidth by the inclusion of a Butterworth filter of order 19. As our heterodyne interferometer is not stabilized, in the simulations in the fourth row the interferometer's phase was optimized to replicate the experimental in-phase component shown in the third row.

We found a good agreement in all the analyzed situations, with the exceptions of (a1) and (e1) as compared to (a2) and (e2), respectively, where the stretching of these waveforms lowers the instantaneous detected power and thus degrades the observed SNR. This effect is more prominent at the 10-mV scale of (a1) and (e1). In addition, these intensity traces show wavy heads or tails, regions that are smoothed by the bandwidth limitation imposed by the RTO and which are only approximately described in the simulation. Globally, the experiment

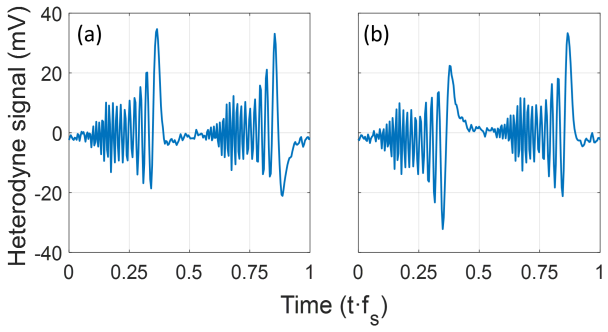

Figure 9. (a) Heterodyne signal at the semi-integer Talbot condition $p/q = 29/2$. (b) Hilbert transform of the heterodyne signal.

captures well the qualitative view described in Fig. 5, with a shortest pulse in the two-sided Airy configuration with main peak FWHM width 210 ps. The field measurements and spectrograms in rows 3 and 5, respectively, clearly show the curvature of the time-frequency parabola (14).

Subsequently, we used heterodyne measurements to quantify the phase of the optical field in the time domain and so confirm the far-field character of the Airy pulses shown in columns (b) and (d) of Fig. 7. In Fig. 8(a) we show the heterodyne signal in blue, together with its temporal phase, in orange, for the single-sided Airy pulse. This phase was fitted to the asymptotic expression given in (11), giving a scale parameter $\kappa = 21.7$ rad/ns$^{3/2}$ in good agreement with the design value of 20.9 rad/ns$^{3/2}$. The situation shown in column (d), which is analyzed in Fig. 8(b), corresponds to a field carried at frequency Ω_B with approximately complex-conjugate envelope. This can be deduced by setting $\Delta\omega = \Omega_B$ in (16) and considering in the limit $\varepsilon \to 0$. The expected asymptotic phase is thus, up to the carrier shift, the opposite to that described in Fig. 8(a). The change in frequency trend is apparent and indeed, after the fit of the retrieved phase, we obtain a carrier of 5.736 GHz, in good agreement with the expected value of 6 GHz, and a negative curvature with $\kappa = -20.4$ rad/ns$^{3/2}$.

We also confirmed that the change of shifting frequency to fractional Talbot conditions $\Omega_s \tau_g = 2\pi \times p/q$ provides Airy pulse trains with q pulses per period, as dictated by fractional Talbot effect. As an example, and using a specific property of semi-integer Talbot conditions, we experimentally resolve the in-phase and quadrature components of the single-sided Airy pulse. At a fractional value $p/q = 29/2$ the phase acquired by the spectral components (7) can be written as:

$$e^{-j\frac{1}{2}\Omega_s \tau_g n^2} = (-j)^{n^2} = \frac{e^{-j\pi/4}}{\sqrt{2}}\left[1 + j(-1)^n\right] \tag{18}$$

The waveform thus contains two replicas of the Airy pulse train, mutually delayed by half a period and with a relative phase factor of j. In a heterodyne measurement, the train appears as a periodic succession of in-phase and minus quadrature components of the electric field within each period. An experimental trace is shown in Fig. 9(a). The relative phase between components is confirmed after Hilbert transforming the heterodyne signal, see Fig. 9(b), which shows how the first pulse (in-phase) in (a) is transformed to quadrature in (b), and

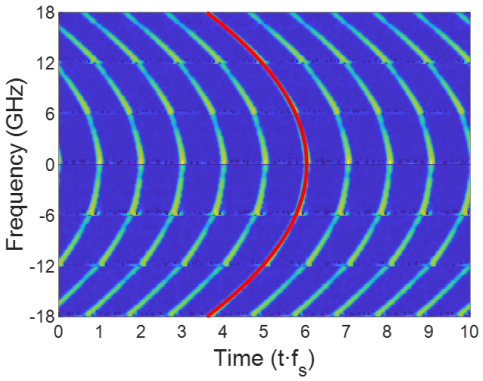

Figure 10. Reconstruction of the time-frequency parabola by temporal and spectral shifts of different spectrograms obtained by detuning the $p = 17$ Airy pulse in steps of 32 kHz. Red curve: parabola (14).

the second pulse in (a) (minus quadrature) is transformed to in-phase in (b).

To conclude our analysis, we observe that (14), together with (10), points out that the spectrograms of all possible Airy fields obtained by detuning the shifting frequency are portions of the same normalized parabola $-2\Omega_s t = |\varphi|\omega_i^2$. In Fig. 10 we present the reconstruction of this curve by adjoining the strips, shifted in time and frequency, that represent the spectrograms of different waveforms. They were obtained by progressively detuning the shifting frequency from the $p = 17$ Talbot waveform in steps of 32 kHz, corresponding to our 6 GHz RTO bandwidth. Comparison with curve (14), shown in red, confirms the correct reconstruction of the Airy parabola.

5.3. Stability

In a final set of experiments, we analyzed the stability in amplitude and timing jitter of the resulting pulse trains. The dominant cause of amplitude noise is ASE, whereas jitter is mainly due to the phase noise of the injected carrier and to technical noise, namely, vibrations and thermal drifts that cause length variations in the fiber loop [44]. These are typically low-frequency effects: values of rms jitter below the ps have been reported both in Talbot lasers [31] and in frequency-shifting loops [44] when integrated above 10 kHz. Active stabilization, in turn, is necessary to improve jitter below the 10-kHz range [44]. In our case, the dominant jitter mechanism in this range is technical noise, as the seed linewidth (< 100 Hz) only contributes to jitter below the ps scale [29].

In the experiments, we used the double-sided Airy pulse configuration of Fig. 7(c). This configuration was chosen because these pulses were observed to be prone to amplitude and timing errors, as all frequencies should add at the same time to create the pulse. In a first series of tests, we explored the stability of the setup without PZT stabilization. The experiments were performed at the $p = 18$ integer Talbot condition with a slightly shorter cavity ($f_s = 85.616$ MHz and $\tau_g = 210.3$ ns). The laser output was directly detected and the RF spectrum of the intensity recorded in a spectrum analyzer. In Fig. 11(a) we show

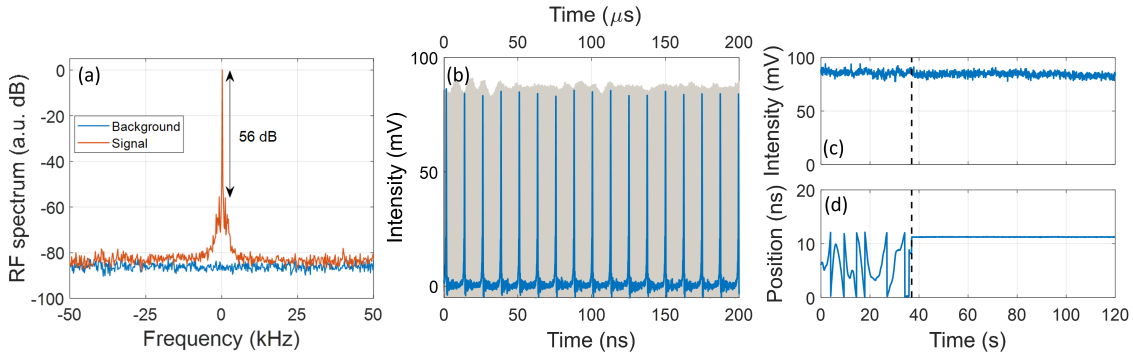

Figure 11. (a) RF spectrum of the fundamental (orange) and noise background (blue) in units relative to the fundamental. Resolution bandwidth 10 Hz. (b) Intensity of a burst of single-sided Airy pulses in a 200-μs interval (gray, top scale, pulses not resolved), and zoom of this trace in a 200-ns interval (blue, bottom scale). (c) Peak intensity and (d) pulse position with respect to the reference RF clock tracked over successive periods during a 120-s interval. The active stabilization is activated at $t = 37$ s, marked with a dashed line. Timing errors are measured within a modulation period $1/f_s = 11.68$ ns.

its fundamental (orange) and the corresponding noise background (blue), with a peak to pedestal value of 56 dB at a resolution bandwidth of 10 Hz. Neglecting the timing jitter contribution to the fundamental, the fluctuations σ_E of the pulse energy E can be expressed as $\sigma_E/E = (P_n/P_f)^{1/2}$, where P_f is the power at the fundamental and P_n is the integrated noise power [61]. This results in a value for $\sigma_E/E = 0.027$, of the order of mode-locked frequency-shifted feedback fiber lasers based on similar architectures [62].

We also explored the intensity and timing jitter noises in the time domain at short time scales. In Fig. 11(b) we show the RTO digitized trace, in gray, of the intensity envelope of a pulse train of 200 μs duration comprising $\sim 16 \times 10^3$ pulses. A short run of 200 ns, extracted from the long trace, is also shown in blue for comparison. The pulse burst shows an acceptable stability: the intensity envelope has a standard deviation $\sigma_I/\bar{I}_p = 0.017$ relative to the average peak intensity $\bar{I}_p$, and the jitter standard deviation was found to be $\sigma_t = 7$ ps.

At longer times scales we observed that the amplitude variations are still low but timing jitter severely degrades, as expected. In Fig. 11(c) and (d) we present, respectively, the observed amplitude and timing jitter fluctuations in a 2-min period before and after activating the feedback control at 37 s. Here, amplitude and timing fluctuations were determined by recording in the RTO a single period of the intensity triggered by the master RF tone at the shifting frequency f_s, and using the RTO utilities for measuring the peak intensity and position in each period. This procedure provides position values with ps resolution. Without active control, pulse jitter appears dominated by low-frequency variations due to thermal drifts in the fiber loop. With the PZT activated, we found that the relative intensity fluctuation is $\sigma_I/\bar{I}_p = 0.024$, in the same range as in the short burst, and a timing jitter of $\sigma_t = 23$ ps. If this jitter is entirely ascribed to loop's length fluctuations, it amounts to a relative loop length variation of $\sigma_t/\tau_g \sim 10^{-4}$, or to a FSR stability < 500 Hz.

6. Conclusions

In this work, we have demonstrated the emission of bandlimited, single-sided ns Airy pulses from a Talbot fiber laser with bandwidths in excess of 10 GHz and ~ 80 MHz-repetition rates. The system has been built upon a stabilized dispersive and active fiber ring cavity incorporating a frequency shifter, where dispersion has been implemented through commercial LCFBGs. The emitted finite-energy pulses lie in the higher-order far-field regime, where the asymptotic behavior dictated by the stationary phase approximation applies. The emission was tunable through changes in the the shifting frequency, which introduces a controlled amount of equivalent first-order dispersion over the Airy pulses. Previous theoretical models have been shown to accurately describe the actual laser output in all the analyzed configurations. We have also identified a method for optimum spectral allocation of the seeding wavelength to minimize ASE recirculation, and evaluated the setup stability in amplitude and timing jitter.

The demonstrated system can be extended in several directions. The requirement of large intracavity first-order dispersion can be alleviated using lower shifting frequencies. Alternative LCFBG designs, with apodization profiles distinct from the flat-topped used here or with narrower passbands, can help set the net gain region for laser operation. Different spectral phase profiles, distinct from the cubic used here, can be induced by the inclusion of more general dispersive delay lines within the loop, and its use in conjunction with intracavity modulators may extend the capacities of Talbot lasers and frequency shifting loops for optical pulse generation. The present approach constitutes, in summary, a compact alternative to external spectral filtering for the generation of pulses with non-conventional spectral and temporal phase characteristics.

Acknowledgments

Grants PID2020-120404GB-I00 funded by MCIN/AEI/ 10.13039/501100011033 and EQC2019-006189-P funded by MCIN/AEI/10.13039/501100011033 and by ERDF *A way of making Europe*. MC is also supported by Ministerio de Universidades, Spain, grant FPU21/05449.

Data Availability Statement

All data that support the findings of this study are included within the article. Additional data are available from the corresponding author upon reasonable request.

References

[1] Chi H and Yao J 2007 *IEEE T. Microw. Theory* **55** 1958–1963
[2] Chi H and Yao J 2008 *J. Lightwave Technol.* **26** 1282–1287
[3] Wang C and Yao J 2008 *IEEE T. Microw. Theory* **56**
[4] Ashrafi R, Park Y and Azaña J 2010 *IEEE T. Microw. Theory* **58** 3312–3319

[5] Asghari M H and Jalali B 2013 *Appl. Opt.* **52** 6735–6743
[6] Jalali B, Chan J and Asghari M H 2014 *Optica* **1** 23–31
[7] Chen C L, Mahjoubfar A and Jalali B 2015 *PLOS ONE* **10** 1–11
[8] Zuo P, Ma D and Chen Y 2023 *Opt. Lett.* **48** 29–32
[9] Tovar P, Ynóquio Herrera L E, Ribeiro R M and von der Weid J P 2019 *IEEE Photonic. Tech. L.* **31** 1417–1420
[10] Hariharan D, Martijn de Sterke C and Runge A F J 2023 *Opt. Express* **31** 21553–21562
[11] Liu S, Zhang Y, Malomed B A and Karimi E 2023 *Nat. Commun.* **14** 222
[12] Malomed B A 2021 *Photonics* **8** 353
[13] Chong A, Renninger W H, Christodoulides D N and Wise F W 2010 *Nature Photon.* **4** 103–106
[14] Abdollahpour D, Suntsov S, Papazoglou D G and Tzortzakis S 2010 *Phys. Rev. Lett.* **105** 253901
[15] Efremidis N K, Chen Z, Segev M and Christodoulides D N 2019 *Optica* **6** 686–701
[16] Bender C and Orszag S 1999 *Asymptotic Methods and Perturbation Theory* (Springer)
[17] Berry M and Balazs N 1979 *Am. J. Phys.* **4** 264–267
[18] Siviloglou G A and Christodoulides D N 2007 *Opt. Lett.* **32** 979–981
[19] Siviloglou G A, Broky J, Dogariu A and Christodoulides D N 2007 *Phys. Rev. Lett.* **99** 213901
[20] Broky J, Siviloglou G A, Dogariu A and Christodoulides D N 2008 *Opt. Express* **16** 12880–12891
[21] Fattal Y, Rudnick A and Marom D M 2011 *Opt. Express* **19** 17298–17307
[22] Ament C, Polynkin P and Moloney J V 2011 *Phys. Rev. Lett.* **107** 243901
[23] Driben R, Hu Y, Chen Z, Malomed B A and Morandotti R 2013 *Opt. Lett.* **38** 2499–2501
[24] Mandeng L M, Tchawoua C, Tagwo H, Zghal M, Cherif R and Mohamadou A 2016 *J. Lightwave Technol.* **34** 5635–5641
[25] Hu Y, Li M, Bongiovanni D, Clerici M, Yao J, Chen Z, Azaña J and Morandotti R 2013 *Opt. Lett.* **38** 380–382
[26] Banerjee A and Roy S 2018 *Phys. Rev. A* **98** 033806
[27] Agrawal G P 2007 *Nonlinear Fiber Optics* (Academic Press)
[28] Guillet de Chatellus H, Jacquin O, Hugon O, Glastre W, Lacot E and Marklof J 2013 *Opt. Express* **21** 15065–15074
[29] Guillet de Chatellus H, Lacot E, Glastre W, Jacquin O and Hugon O 2013 *Phys. Rev. A* **88**(3) 033828
[30] Wang L and LaRochelle S 2017 Talbot laser with tunable GHz repetition rate using an electro-optic frequency shifter *2017 Conference on Lasers and Electro-Optics (CLEO)* pp 1–2
[31] Billault V, Crozatier V, Baili G, Feugnet G, Schwarz M, Nouchi P, Dolfi D and Guillet de Chatellus H 2019 *IEEE Photonic. Technol. L.* **31** 1842–1845
[32] Yatsenko L, Shore B and Bergmann K 2004 *Opt. Commun.* **236** 183–202
[33] Guillet de Chatellus H, Romero Cortés L, Schnébelin C, Burla M and Azaña J 2018 *Nat. Commun.* **9** 2438
[34] Shimizu K, Horiguchi T and Koyamada Y 1992 *Opt. Lett.* **17** 1307–1309
[35] Zhang Y, Liu C, Shao K, Li Z and Pan S 2020 *Opt. Lett.* **45** 2038–2041
[36] Lyu Y, Li Y, Yu C, Yi L, Nagatsuma T and Zheng Z 2022 *J. Lightwave Technol.* **40** 1036–1042
[37] Chen T, Kong W, Liu H and Shu R 2018 *Opt. Express* **26** 34753–34762
[38] Ogden H M, CMurray J B, Murray M J and Redding B 2023 *Sci. Rep.* **13** 5762
[39] Zhang Y, Liu C, Zhang Y, Shao K, Ma C, Li L, Sun L, Li S and Pan S 2021 *J. Lightwave Technol.* **39** 458–464
[40] Liu Y, Zhang Z, Burla M and Eggleton B J 2022 *Laser Photonics Rev.* **16** 2100549
[41] Zhang Z, Lui Y, Stephens T and Eggleton B J 2023 *Nat. Photonics* **17** 791–797
[42] Zhang Z, Liu Y, Magi E and Eggleton B J 2024 *Opt. Lett.* **49** 3818–3821
[43] Yang H, Vallet M, Zhang H, Zhao C and Brunel M 2019 *Opt. Express* **27** 18766–18775
[44] Billault V, Crozatier V, Baili G, Morvan L, Dolfi D, Kanagaraj N and Guillet de Chatellus H 2021 *J. Lightwave Technol.* **39** 2336–2347
[45] Lyu W, Tian H, Fu Z, Zhang L, Zeng Z, Zhang Z, Zhang S, Li H and Liu Y 2023 *Opt. Lett.* **48** 3411–3414
[46] Yang H, Wang L, Zhao C and Zhang H 2021 *J. Lightwave Technol.* **39** 3112–3120
[47] Brunel M, Frein L, Carré A, Le Beux T, Tolba N, Alouini M, Guillet de Chatellus H, Vallet M *et al.*

2023 Nonlinear frequency chirps from a stabilized injected phase-modulated fiber laser loop *EPJ Web of Conferences* vol 287 (EDP Sciences) p 07015
[48] Clement J, Guillet de Chatellus H and Fernández-Pousa C R 2020 *Opt. Express* **28** 12977–12997
[49] Preciado M A and Muriel M A 2012 *J. Lightwave Technol.* **30** 3660–3666
[50] Kanagaraj N, Djevarhidjian L, Durán V, Schnébelin C and Guillet de Chatellus H 2019 *Opt. Express* **27** 14842–14852
[51] Fernández-Pousa C R and Guillet de Chatellus H 2022 *J. Lightwave Technol.* **40** 6831–6844
[52] F W J Olver, A B Olde Daalhuis, D W Lozier, B I Schneider, R F Boisvert, C W Clark, B R Miller, B V Saunders, H S Cohl, and M A McClain, eds NIST digital library of mathematical functions `https://dlmf.nist.gov/`, Release 1.2.0 of 2024-03-15
[53] Cuenca M, Maestre H, Torregrosa G, Guillet de Chatellus H and Fernández-Pousa C R 2023 *Opt. Express* **31** 15615–15636
[54] Sabert H and Brinkmeyer E 1994 *J. Lightwave Technol.* **12** 1360–1368
[55] Cuenca M, Maestre H and Fernández-Pousa C R 2024 *Opt. Lett.* **49** 1005–1008
[56] Azaña J and Muriel M A 2001 *IEEE J. Sel. Top. Quant.* **7** 728–744
[57] Cortés L R, Guillet de Chatellus H and Azaña J 2016 *Opt. Lett.* **41** 340–343
[58] Fernández-Pousa C R 2017 *J. Opt. Soc. Am. A* **34** 732–742
[59] Poladian L 2000 *Appl. Opt.* **39** 1920–1923
[60] Sumetsky M, Eggleton B J and Martijn de Sterke C 2002 *Opt. Express* **10** 332–340
[61] von der Linde D 1986 *Appl. Phys. B* **39** 201–217
[62] Woodward R I, Majewski M R and Jackson S D 2018 *APL Photonics* **3** 116106